How to Cite: Bondarenko, L.S., Dzeranov, A.A., Tropskaya, N.S., & Kydralieva, K.A. (2026). Dispersion Technique May Change Structure and Bio-Oxidative Activity of Magnetic MOF Nanoparticles. *Eurasian Journal of Chemistry, 31, 1(121), 151–163.* https://doi.org/10.31489/2959-0663/1-26-8

Article

Received: 2 December 2025 | Revised: 2 March 2026 | Accepted: 5 March 2026 | Published online: 13 March 2026

UDC 544.42+519.242.7

https://doi.org/10.31489/2959-0663/1-26-8

Lyubov S. Bondarenko[1], Artur A. Dzeranov[1], Nataliya S. Tropskaya[1, 2], Kamila A. Kydralieva[1*]

[1]*Moscow Aviation Institute (National Research University), Moscow, Russia;*
[2]*Sklifosovsky Research Institute for Emergency Medicine, Moscow, Russia*
*(*Corresponding author's e-mail: kamila.kydralieva@gmail.com)*

Dispersion Technique May Change Structure and Bio-Oxidative Activity of Magnetic MOF Nanoparticles

The overlooked influence of routine operations on hydrophobic nanosuspensions can induce polymorphic transformation, a critical factor that contributes to their instability and significantly limits their applications. Techniques such as ultrasonication are commercially employed for producing nanosuspensions. However, the impact of routine operations, including mechanical grinding and ultrasound, on obtaining stable suspensions has not received sufficient attention, despite their potential to alter microstructure, morphology, and consequently, functional properties. In this study, Fe_3O_4-ascorbic acid/ metal-organic coordination polymer (MOF) MIL-88b (Fe_3O_4-AA-MOF) nanoparticles (NPs) were subjected to grinding in a mortar (GM). Subsequently, 1.0 wt.% of aqueous suspensions were ultrasonicated (GM+US) for 3 min at 30 kHz and 37 °C. The structure and oxidative properties of the homogenized suspensions were investigated using X-ray diffraction technique, dynamic light scattering (DLS), and scanning electronic microscope (SEM), with native NPs serving as a control. Homogenization treatment significantly affected the microstructure and oxidative behavior of Fe_3O_4-AA-MOF NPs. The combination of milling and ultrasound led to a change in the stoichiometry of magnetite, partial destruction of MOF, and simultaneously, an acceleration of the Fenton reaction and increased stability of NPs in suspension. These findings underscore that the influence of routine sample preparation operations on the functional properties of NPs cannot be underestimated.

Keywords: metal organic framework, MOF, magnetic iron oxide nanoparticles, nanosuspensions, sample preparation operations, grinding in the mortar, ultrasonication, structure, oxidative properties

Introduction

The reproducibility crisis of scientific experiments can stem from various factors affecting chemical reactions, including solvent variability, temperature fluctuations, vessel configuration, heat and mass transfer within the reaction mixture, challenges with thorough mixing, reagent and intermediates purity, and contamination or phantom reactivity, as highlighted by [1]. However, another often-overlooked factor significantly impacting the reproducibility of biological experiments, particularly those involving insoluble chemical compounds like magnetite nanoparticles (NPs), is the mandatory sample preparation. These routine operations, justified by the logic of *in vitro* and *in vivo* experiments, include grinding samples and dispersing them to achieve the required sizes for administration, such as intravenous injection. Such operations are frequently considered so routine and insignificant that they are often omitted from experimental methodology. Nevertheless, they can induce changes not only in particle size but also in their microstructure and, consequently, their functional properties.

In a recent Nanofocus paper [2], the authors identified the need for improved nanotechnology tools and methods as one of 33 key questions in nanoscience and nanotechnology. As a crucial characteristic of NPs, size profoundly influences the efficiency of passive or active targeted drug delivery and other biomedicine applications. This influence extends to circulation time, biodistribution, accumulation, and penetration, cellular uptake, and subcellular distribution [3, 4]. While the preferred size for intravenous injection typically ranges from 2 to 200 nm, as larger NPs (>200 nm) are prone to phagocytosis by macrophages and thus cannot leverage the enhanced permeability and retention effect [5, 6]. NPs generally range from 10 to 1000 nm in size [7]. Furthermore, numerous properties, including size, dictate their *in vivo* behavior, encompassing stability in blood and other body fluids, biodistribution, margination, circulation time, phagocytic uptake, organ-specific accumulation, drug release, attachment and penetration into target cells, excretion and toxicity

[3, 5, 6, 8–12]. Stability is a critical prerequisite for most of the biopreparations, as it ensures predictable and controllable behavior. Consequently, nanofluids are desired to possess thermodynamic, kinetic, chemical, and dispersion stabilities. Due to inter-particle adhesion forces, NPs tend to agglomerate, and their settlement can occur due to the gravitational forces [13]. Concurrently, an increasing number of newly developed drugs exhibit poorly solubility, leading to bioavailability challenges. A promising alternative approach to overcome these issues is the production of stable nanosuspensions with controlled size or post-production processing of NPs [14]. To prepare stable nanofluids, extensive investigations into colloidal dispersions have been conducted, focusing on particle motion analysis under various flow conditions and sedimentation characteristics of suspended NPs in base fluids [15]. Two primary methods exist for producing nanofluids; (i) the one-step direct evaporation method, which involves the direct formation of NPs within the base fluids, and (ii) the two-step method, which entails forming NPs and subsequently dispersing them in the base fluids [15]. In the latter approach, various dispersion techniques are employed, including stirrers, ultrasonic baths, ultrasonic disruptors, high-pressure homogenizers, and modified magnetron sputtering systems, to prepare nanofluids. Among these techniques, ultrasonication is widely used [13] due to its technical simplicity and cost effectiveness. During homogenization, particle fracture is achieved through cavitation, high-shear forces, and inter-particle collisions [16]. It is commonly assumed that longer ultrasonication durations are more beneficial for nanofluid preparation [13]. However, no standardized protocols have been established to nanofluid preparation, particularly regarding optimal homogenization duration, sonicator power amplitude, or the type and duration of pulse mode operation. Nevertheless, the National Institute of Standards and Technology (NIST, Gaithersburg, MD), in collaboration with the Center for the Environmental Implications of Nanotechnology (CEINT of Duke University), has initiated efforts to develop standardized and validated protocols for NPs dispersion [17]. Proposed guidelines include the use of cooling baths, pulse mode operation, and cylindrical flat-bottom beakers. It is important to note that ultrasonication is a complex physicochemical process that can both break down agglomeration and induce further aggregation, alongside other effects together and chemical reactions [17]. For iron-containing nanoparticles, even trace water and dissolved oxygen can shift the oxidation pathway and kinetics, as shown for zerovalent iron nanoparticles in isopropanol where the presence of water and air governs the transformation into oxide particles [18]. Ultrasonic dispersion is also frequently employed to obtain stable nanosuspensions for biomedicine [19–21]. Despite its routine use, authors often overlook the state of NPs microstructure after dispersion. The harsh effect of cavitation can not only lead to re-aggregation [17], but also cause a change in the sample's microstructure and surface chemistry [22]. According to Li et al [22], ultrasonic irradiation can alter the dealloying process, activate particles by removing the oxide layer, and influence the morphology and structure of the products. Li et al. demonstrated that ultrasonic irradiation leads to chemical dealloying of Co-Al NPs. Similarly, Zhang et al [23] showed that extensive sonication severely damages the crystal structures of carbon nanotubes, thereby degrading the mechanical properties of carbon nanotube films and their composites. However, we have found no studies investigating the structure and functional properties of NPs after ultrasonic dispersion specifically for injection applications.

Iron-based metal-organic coordination frameworks (MOFs) serve as efficient catalysts for heterogeneous Fenton reactions due to their high porosity, large specific surface area, and numerous, uniformly distributed unsaturated iron sites [24, 25]. We utilized, MIL-88b (Fe), a three-dimensional porous MOF composed of 1,4-benzenedicarboxylic acid and octahedral trinuclear Fe clusters (Fe_3-μ_3-oxo) with vacant coordination sites accessible to hydrogen peroxide (H_2O_2) molecules. The resulting MIL-88b was modified with ascorbic acid (AA) to accelerate the Fe^{2+}/Fe^{3+} redox cycle and iron oxides, particularly magnetite Fe_3O_4, for localized drug delivery [26]. In this study, an aqueous suspension of Fe_3O_4-AA-MOF was homogenized using a mechanical grinding and ultrasound treatment as a routine procedure for injection. The effect of this homogenization, as a sample preparation step for injection, on both the crystal structure and oxidative characteristics of NP_S was investigated.

Experimental

Preparation of the Fe_3O_4-AA-MOF

The Fe_3O_4-AA-MOF complex was synthesized following a procedure as described in [26]. Briefly, The Fe_3O_4–MOF complex was prepared in an inert atmosphere (argon) in two steps. In the first step, magnetite NPs were obtained by coprecipitation of aqueous solutions of iron(II) and iron(III) salts with a base using the Elmore method [27] in an inert atmosphere (argon). Briefly, 3.07 g $FeCl_3 \times 6H_2O$ and 1.13 g $FeSO_4 \times 7H_2O$ were dissolved in 0.35 L of deionized water and stirred using a mechanical stirrer (1400–1500 rpm). Then

6.8 mL of 25 % NH_4OH solution were slowly added with stirring, adjusting the pH to 9. Then, ascorbic acid (0.1 g AA per 1 g MOF), 5.90 g (0.035 mol) terephthalic acid (TPA) and 8.70 g (0.0118 mol) $[Fe_3O(C_8H_4O_4)_3(H_2O)_3]Cl$ were added to the suspension containing magnetite NPs. The mixture was continuously stirred with a mechanical stirrer (900 rpm) for 60 min. The precipitate was filtered off on a paper filter and washed repeatedly with degassed distilled water and 96.5 % ethanol. The resulting sample was dried in a dynamic vacuum at low heating (60 °C). Elemental analysis revealed an iron content of 44.4 %. Infrared spectroscopy (KBr pellet) confirmed the expected structure, with characteristic peaks observed at 3423 cm^{-1} (O–H), 2925 cm^{-1} (CH), 1564 and 1392 cm^{-1} (COO–), 1155 cm^{-1}, and 1018, 822, 749, 613, and 551 cm^{-1} (Fe–O).

Pretreatment

Intravenous administration of NPs requires their dispersion to reduce their size: dispersion was carried out sequentially by the gentle manual grinding in an agate mortar using agate pestle for 10 min in air-ambient conditions and/or treatment in an ultrasonic bath (30 kHz, 50 W) for 3 min at 37 °C. Thus, three samples were selected for subsequent analysis of structure and morphology: initial Fe_3O_4-AA-MOF (IN), after grinding in the mortar (GM) and after both grinding and ultrasonication (GM+US).

X-Ray Diffraction Analysis

Transmission geometry was used for X-ray diffraction (XRD) analysis on a Philips X-pert diffractometer (Philips Analytical, Eindhoven, The Netherlands) with Cr-Ka radiation (λ = 2.29106 Å) and a step size of 0.0121. Quantitative analyses were performed by refinement of the total multiphase spectrum method (the Rietveld method) with a fundamental parameters approach, using the Profex software. Background was handly calculated and a fixed seven-line K_α plus an intensity-refined K_β emission profile was adopted.

Fourier Transform Infrared Spectroscopy

The functional groups present in the samples were analyzed using Fourier transform infrared (FTIR) spectroscopy. Measurements were performed on an FTIR IR-200 spectrometer (ThermoNicolet, Waltham, MA, USA) in the range of 4000 to 400 cm^{-1}. For analysis, powdered samples were mixed with high purity potassium bromide (KBr) at a ratio of 1 mg sample to 150 mg KBr. The mixture was then pressed into pellets with a diameter of 13 mm using a force of 6 tons.

Scanning Electron Microscopy

To examine the size and shape of the particles, we used scanning electron microscopy (SEM). First, a double-sided sticky tape was attached to small sample holders (SEM stubs), and the particles were placed onto the stubs. To enhance image quality, a thin layer of platinum (10 nm thick) was sputtered onto the samples. Finally, the particles were observed using a Tescan Vega 3 microscope operating at 20 kV, equipped with a specialized detector for secondary electrons.

Determining the Degree of Methylene Blue Decolorization.

The degree of methylene blue decolorization was assessed as an indirect indicator of OH-radicals production during the Fenton reaction (H_2O_2 decomposition) using UV-Vis spectroscopy. This method relies on the colour change of MB caused by these radicals. The experiments were carried out under conditions simulating the microenvironment of tumor cells 0.1 M buffers (NaAc for pH 4.5) [28, 29]. Briefly, 10 mg of the sample was suspended in 1.5 mL of 0.1 M buffers (NaAc for pH 4.5) and MB. The mixture was heated to 37 °C and stirred at 700 rpm. 30 % H_2O_2 (100 mM) was then added to initiate the Fenton reaction. To enable comparison of the experimental results with literature data, the H_2O_2 concentration was chosen in accordance with model experiments by other authors [30, 31]. At specific points in time (0, 30, 90, and 180 min), the reaction was stopped, and the supernatant was separated by centrifugation at 6000 rpm for 2 min. The absorbance of the supernatant was measured at 652 nm using a Cary UV-Vis-NIR Spectrophotometer (Agilent Technologies).

Determination of the Equilibrium Concentration of Fe^{2+} and Fe^{3+} in Solution

To detect iron ions, the powder was suspended in 0.1 M buffers (NaAc for pH 4.5) then subjected to centrifugation (6000 rpm, 5 min) after 0, 30, 90, 180 min, and 24 h. Appropriate ion detection reagents were added to the supernatant after separation. To detect Fe^{3+}, 200 μL of potassium thiocyanate KSCN (50 % solution) and 200 μL of HCl (18.25 % solution) were added to 5 mL of supernatant since the reaction between Fe^{3+} and KSCN proceeded in a strongly acidic medium at pH close to 2. The solution was then kept for

20 min to reach equilibrium, and the absorption spectrum in the region of 480 nm was measured. In order to detect Fe^{2+} ions, 2 mL o-phenanthroline $C_{12}H_8N_2$ H_2O (2.5 % solution) and 600 μL of ammonium acetate buffer solution (250 mL of NH_4OH and 900 mL of glacial acetic acid) were also added to 5 mL of the supernatant. The solution was also kept for 20 min to reach equilibrium (no color change) and examined in the region of 510 nm. The absorbance was detected by UV-Vis-NIR spectrophotometry (Cary UV-Vis-NIR Spectrophotometer, Agilent Technologies).

Results and Discussion

Effect of Sample Preparation on the Crystal Structure and Morphology of NPs

The NPs powder underwent sample preparation, which involved grinding in a mortar followed by dispersion in deionized water using an ultrasonic bath for 3 min at 30 kHz and 37 °C. Our primary interest was to determine whether this sample preparation alters the structure and morphology of the NPs, as such changes could subsequently affect their functional properties. The Fe^{2+} located at tetrahedral sites on the surface of magnetite NPs are highly susceptible to rapid oxidation under ambient conditions, leading to alterations in composition and properties [32]. This sensitivity to oxygen often restricts their application, as distinct magnetic properties and particle size can be compromised. To accurately determine the Fe^{2+}/Fe^{3+} ratio in our samples, employed X-ray diffraction (XRD) analysis (Figure 1), which can reveal changes in the crystal structure indicative of a complete atomic rearrangement that occurs during the oxidation process. As evident from the diffraction pattern, peaks observed at 2θ values of 30.14, 35.53, 43.32, 53.51, 57.20, and 62.69 correspond to those of magnetite (ICDD-PDF 19–629). Additionally, peaks at 17.37, 25.20, and 27.91 correspond to an impurity phase, specifically unreacted TPA ligand (CCDC 1269122). This impurity may be attributed to the entrapment of ligand molecules within the pores of MOF. Low intensity peaks at 39.6° and 41.1° are highly likely due to NH_4Cl (ICDD 34-0710), which was formed as a by-product of the reaction between ferric chloride and ammonia.

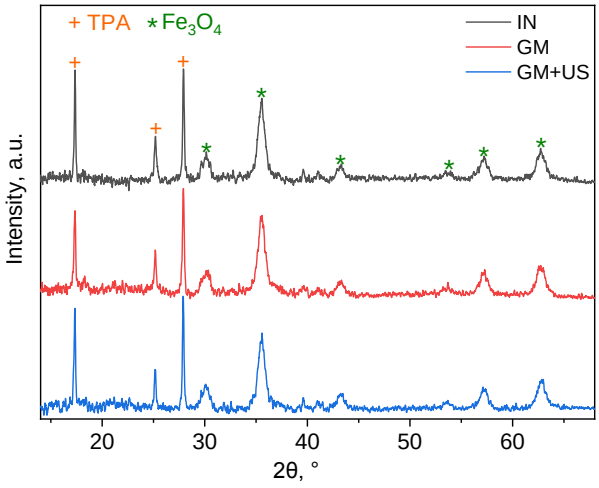

Figure 1. XRD of initial sample (IN), after grinding in the mortar (GM) and after both grinding and ultrasonication (GM+US)

Rietveld analysis, performed using Profex 2.5.4 program (goodness of fit, GoF) values are presented in Table 1), was used to determine the lattice parameters for samples containing iron oxide NPs. Interestingly, all samples displayed lower lattice parameters compared to standard magnetite (8.396–8.400 Å according to ICDD-PDF 19–629), yet higher values than those of maghemite (8.330–8.340 Å according to ICDD-PDF 39-1346). This observation suggests partial oxidation of Fe^{2+} during drying, storage, or modification, leading to the formation of non-stoichiometric magnetite. Stoichiometric magnetite refers to the mineral phase with an ideal Fe^{2+} content, corresponding to the Fe_3O_4 formula. As magnetite undergoes oxidation, its Fe^{2+}/Fe^{3+} ratio changes, resulting in a nonstoichiometric or partially oxidized form, represented by the formula $Fe_{3-\sigma}O_4$ (where σ ranges from zero for stoichiometric magnetite to 1/3 for fully oxidized maghemite) [33].

Table 1

XRD and statistical parameters of Rietveld refinement

	Unit lattice, Å	GOF	Formula
IN	8.3756±0.0002	1.06	$Fe_{2.89}O_4$
GM	8.3742±0.0004	1.07	$Fe_{2.89}O_4$
GM+US	8.3574±0.0001	1.09	$Fe_{2.79}O_4$

This analysis confirms the formation of non-stoichiometric magnetite $Fe_{2.89}O_4$ within the MOF matrix, which contains both magnetite and maghemite NPs (Figure 1). This is likely due to the oxidation of Fe^{2+} ions in the pre-synthesized magnetite. The synthesis, storage, and use of iron oxide NPs can lead to oxidation and phase transformations. The mechanism for this process involves: (1) adsorption of oxygen: oxygen adsorbs onto the NPs surface, where it is ionized by the electrons released during the oxidation of Fe^{2+} to Fe^{3+}, (2) concentration gradient and diffusion: further surface oxidation creates a concentration gradient, promoting diffusion of iron ions to the surface and the formation of vacancies [34]. Gentle manual grinding of NPs in a mortar does not significantly alter the elementary cell parameter or magnetite content (Table 1). In contrast, ultrasonic dispersion results in a notable change in the unit cell parameter, indicating partial oxidation of Fe^{2+} to Fe^{3+} and the subsequent transformation of Fe_3O_4 to γ-Fe_2O_3. This partial oxidation of divalent iron ions may be attributed to the unique conditions of ultrasonic irradiation, such as the acoustic cavitation process, which generates localized hot spots with temperature up to 5000 K, pressures up to 2000 atm, cooling rates of 1010 K s^{-1}. In addition to these hot spots, sonochemical processes also produce shock waves and microjets [35]. Interestingly, while US-exposure can lead to magnetite oxidation, possibly due to the mechanical effects of cavitation, it can also induce the reduction of iron ions depending on the specific conditions. For example, Stolyar et al [36] reported the formation of α-Fe metal phase from iron oxide and iron oxyhydroxide NPs when exposed to ultrasound, but only in the presence of albumin.

As revealed by Infrared (IR) spectroscopy (Figure 2), all three samples exhibited identical absorption bands before and after pretreatment, which demonstrates the stability of the sample's microstructure to both mechanical and ultrasound treatment. In all samples, a broad absorption band in the 2800–3600 cm^{-1} region was observed. This band is attributed to the stretching vibrations of hydroxyl (OH) groups, originating from both physically adsorbed and crystallizing water molecules.

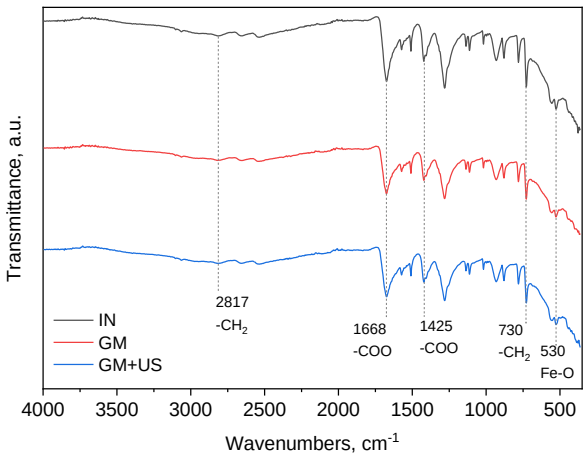

Figure 2. IR-spectra of initial sample (IN), after grinding in the mortar (GM) and after both grinding and ultrasonication (GM+US)

The IR-spectra displayed stretching vibration peaks correspondimg to the =C–H bonds of the terephtaluic acid (TPA) molecules between 2950 and 2640 cm^{-1}, with the most prominent at 2817 cm^{-1}). Additionally, peaks approximately 1600 cm^{-1} and ~1400 cm^{-1} are assigned to the asymmetric and symmetric stretching vibrations of the carboxylate anion (–COO) within the MOF. A vibration peak located at approximately 530 cm^{-1} correspond to the Fe–O bond, which is present in both the MOF and the iron oxide components.

SEM analysis (Figure 3) confirmed that the morphology of Fe_3O_4-AA-MOF was preserved after grinding in a mortar. As shown in Figures 3*a* and *b*, the characteristic bipyramidal shape of the MIL-88B component remained intact [37–39].

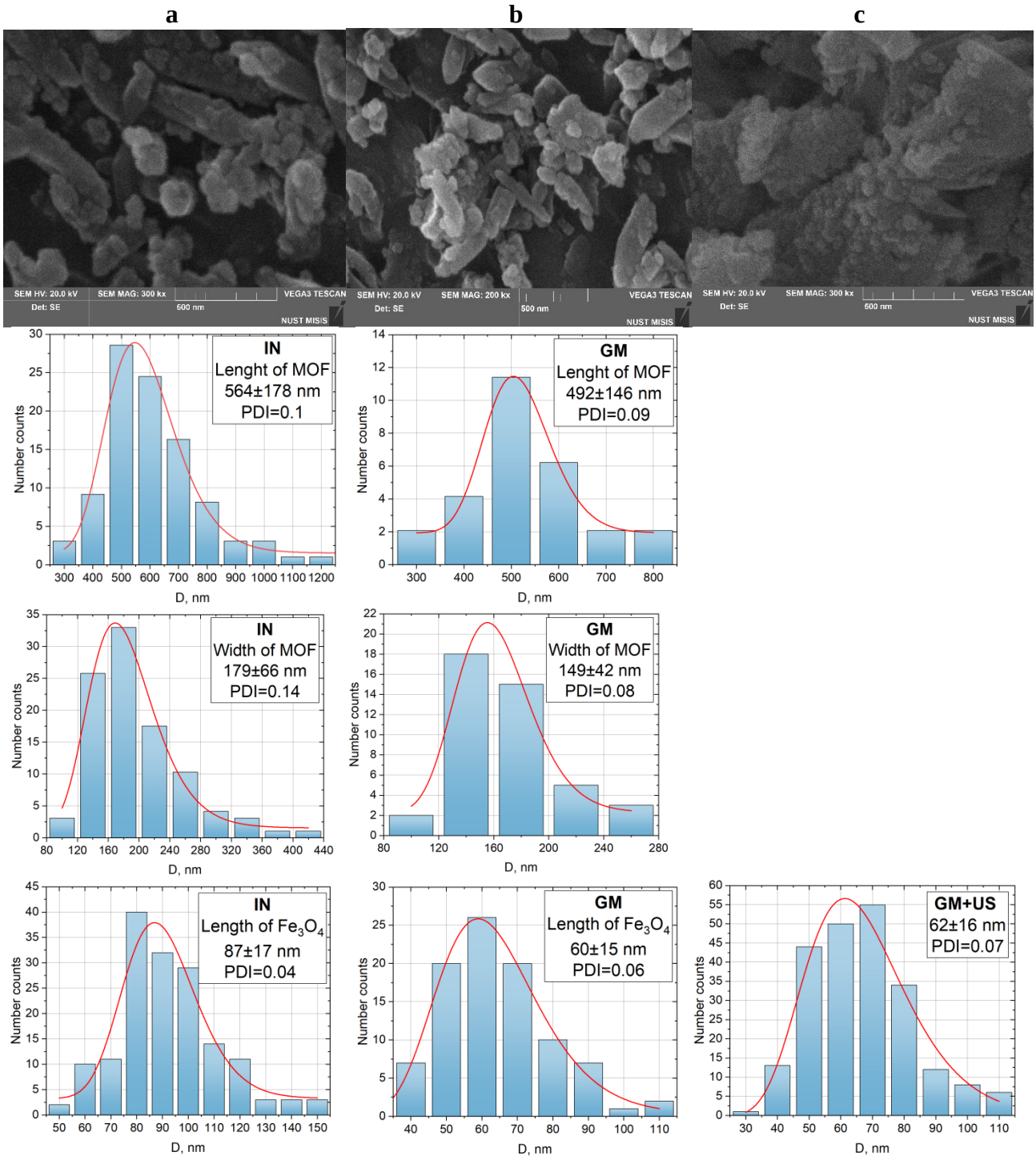

Figure 3. SEM images of IN (*a*) [26], GM (*b*) and GM+US (*c*).
The size distribution for MOF length and width is based on the analysis
of at least 100 particles per image, with at least three images used for each calculation.
(PDI=0 — monodisperse distribution; PDI=1 — polydisperse distribution)

Following the mechanical dispersion, the average particle length decreased from 564 to 492 nm, and the width decreased from 179 to 149 nm. In contrast, subsequent dispersion in an ultrasonic bath resulted in the

partial destruction of the MOF structures (Figure 3*c*), although the iron oxide immobilized on its surface was preserved. The size of these Fe_3O_4 particles was measured to be 62 nm.

To evaluate the stability of the Fe_3O_4-AA-MOF in 0.9 % NaCl solution following the treatments, the concentration of TPA was monitored. The samples were suspended for 180 min with continuous shaking at 300 rpm (Figures 4*a* and *b*).

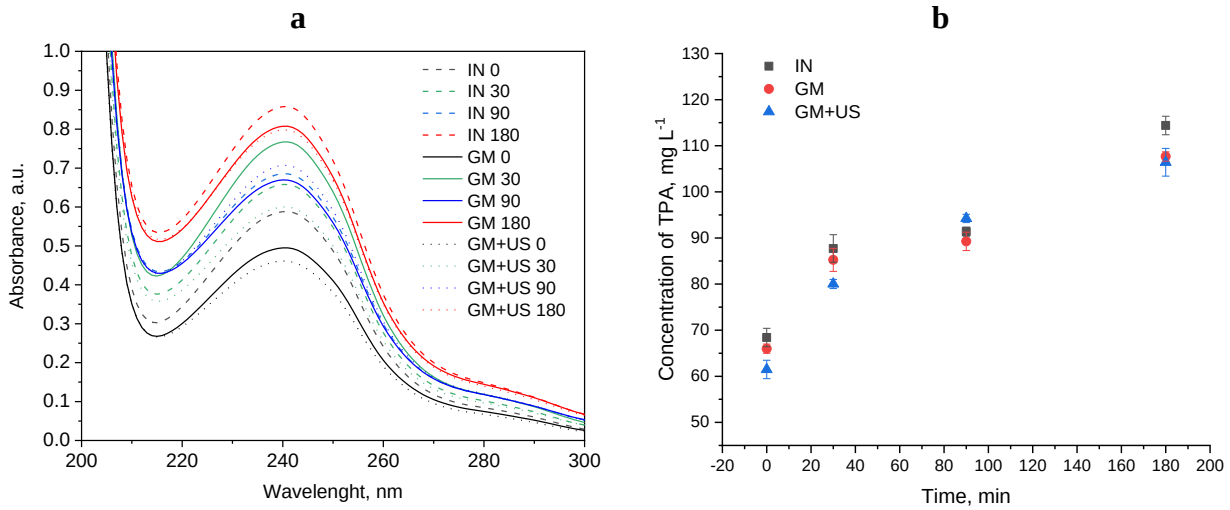

Figure 4. UV-Vis spectra of the samples after grinding in a mortar and dispersion in an ultrasonic bath during 180 min (*a*); Concentration of TPA in IN, GM, GM + US samples during 180 min (*b*)

As shown in Figure 4*b*, the concentration of TPA increased by a factor of approximately 1.7 over the three-hour period. This increase is likely attributable to the release of unreacted TPA from the pores of the MOF, a funding that is consistent with the X-ray diffraction data. Concurrently, the variation in TPA concentration between the untreated and treated samples did not exceed 20 %. This limited variation indicates the sample's stability against both mechanical and ultrasound exposure, which corroborates the findings from IR spectroscopy and X-ray diffraction analyses.

Study of Prooxidant Properties of the Sample Before and After Treatment

In this study, methylene blue (MB) was selected as a model dye to systematically investigate the degradation mechanism and reactive oxygen species (ROS) generation in iron-containing systems. A reduction in absorbance at λ_{max} is typically associated with the oxidation of the chromophore group by hydroxyl radicals (•OH). Dye decolorization was monitored by measuring the decrease in absorbance at its characteristic wavelength of λ_{max} (652 nm) under the experimental conditions suggesting that the dye was likely converted into colorless, smaller molecules [40]. To correlate the model data with the *in vivo* experimental results, sample concentrations of 7.5 and 15 g L^{-1} were chosen, corresponding to doses of 25 and 50 mg kg^{-1}.

An investigation into the effect of sample preparation method used in *in vivo* experiments revealed that mechanical grinding in a mortar, or mechanical treatment followed by ultrasonic dispersion, led to a two-fold increase in the reaction rate. Complete decolorization occurred within 90 min, compared to 180 min for the native sample (Figure S1, SI).

Mechanical dispersion in a mortar resulted in a statistically significant 1.4-fold increase in the Fenton reaction rate. The rate constant increased from 0.015 min^{-1} for the native sample to 0.02 min^{-1} for the ground sample (Figure 5). Conversely, additional dispersion in an ultrasonic bath did not lead to statistically significant changes in the prooxidant properties or any deterioration compared to the original preparation.

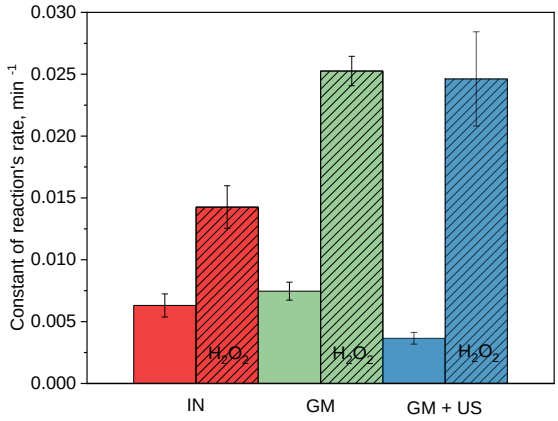

Figure 5. Fenton reaction rate constant of samples in the presence of hydrogen peroxide

The contribution of the Fenton reaction to MB degradation was estimated by calculating the difference between the supernatant absorbance after sorption without H_2O_2 and its absorbance after the Fenton reaction in the presence of H_2O_2. It was observed that both mechanical grinding and a combination of grinding with ultrasonic dispersion resulted in a statistically significant acceleration of the Fenton reaction. It is well-documented that coupling the Fenton reaction with external energy sources like ultraviolet (UV) or ultrasound (US) is of great interest due to a higher yield of hydroxyl •OH radicals or the ability to use lower concentrations of Fenton reagents [41]. Accordingly, the oxidation rate of a process like UV/Fenton is accelerated through generation of additional radical •OH radicals within the system [42, 43].

To elucidate the mechanism underlying the effect of sample preparation on the prooxidant properties of the Fe_3O_4-AA-MOF sample, the release of Fe^{2+} and Fe^{3+} ions was investigated. As illustrated in the corresponding graph, sample preparation generally leads to an increased concentration of both released Fe^{2+} and Fe^{3+} ions over the course of the experiment. Figure 6 shows an estimate of the Fe^{2+}/Fe^{3+} ion ratios for different sample preparation methods 90 minutes after the experiment began. The data indicate that mechanical grinding, as well as its combination with ultrasonic dispersion, leads to a decrease in the relative Fe^{2+} concentration. This is presumably due to the oxidation of these ions in localized hot spots generated by the sonochemical process. Nevertheless, despite the oxidation of Fe^{2+} ions during sample preparation, the net increase in the total concentration of released ions leads to the observed acceleration of the Fenton reaction (Figure 6).

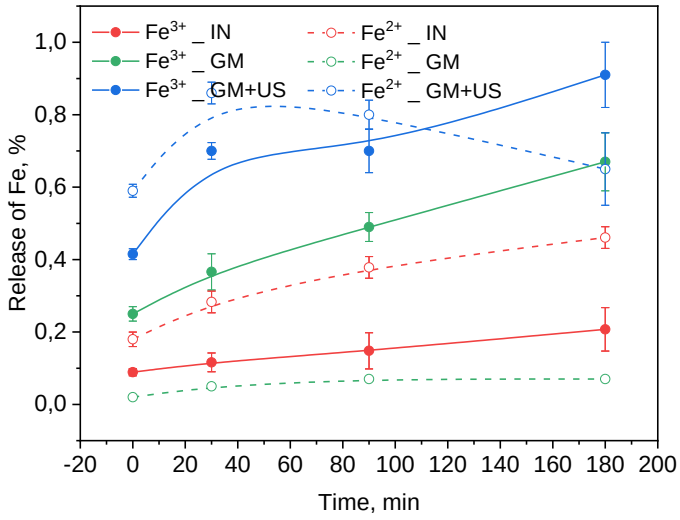

Figure 6. Kinetics of Fe^{2+} and Fe^{3+} release from Fe_3O_4-AA-MOF before and after sample preparation

Several additional reasons for the increased catalytic activity of magnetite NPs are highlighted in the literature. Changes in the catalytic activity of the modified magnetite have been attributed to the existence of thermodynamically favorable redox pairs of cations on the catalysts surface. These pairs are reported to en-

hance Fenton degradation of probe molecules through three primary pethways (i) direct involvement in the Fenton oxidation cycle and generation of •OH radicals via the Haber-Weiss mechanism; (ii) the regeneration of Fe^{2+} cations; and (iii) the acceleration of electron transfer during the oxidation reaction within the magnetite structure [44, 45]. Futhermore, Costa et al. proposed the generation of oxygen vacancies as another possible reason for enhanced catalytic activities [46]. These vacancies, which arise from adjustments for unequal replacements or cationic deficiency in the modified iron oxide structure, can act as active sites. They may contribute either directly to the degradation of probe molecules or indirectly by facilitating the decomposition of H_2O_2 [47]. Additional factors, such as enlarged surface area and consequently higher concentrations of hydroxyl groups on the catalyst surface, have also been reported in numerous studies [48]. Regarding the MOF component, under ultrasonic conditions, MIL-88B can be stimulated to produce electron-hole (e^-h^+) pairs. The resulting electrons can react with O_2 to generate superoxide radicals ($•O_2^-$), while the holes can react with OH^- or H_2O to generate hydroxyl radicals (•OH), also leading to an acceleration of the Fenton reaction [49].

It can be concluded that the observed enhancement of iron ions release and functional properties is caused by the samples preparation steps of mortar grinding and subsequent dispersion. This outcome is likely the result of a decrease in particle size and a corresponding increase in surface area, or the partial destruction of the MOF. These changes would create more active sites on the surface for contact with H_2O_2 and promote the release of Fe^{2+}/Fe^{3+} ions.

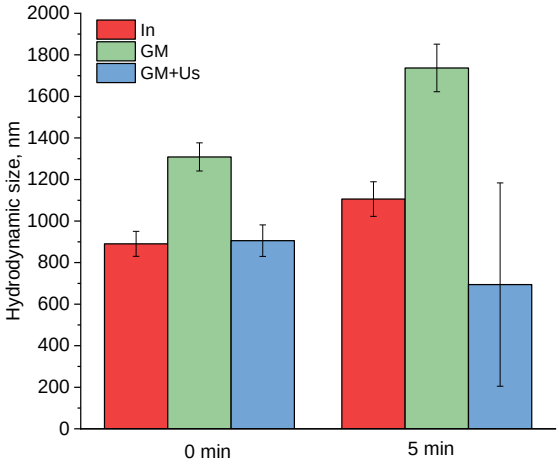

Figure 7. Change in hydrodynamic diameter of NPs before and after treatment for 5 min

The hydrodynamic diameter of NPs was evaluated by DLS in 0.9 % NaCl medium, as shown in Figure 7. A particle size distribution analysis in deionized water confirmed that all prepared samples were polydisperse, exhibiting polydispersity indices between 0.004 and 0.007. The initial average particle diameters at time zero were measured as 890±60 nm for the initial NPs (IN), 1308±83 nm for particles subjected to grinding in a mortar (GM), and 906±76 nm for particles that were ground and subsequently treated with ultrasonication (GM+US). The untreated NPs consisted of two primary fractions with sizes around 800 nm and 4000 nm. The process of grinding in a mortar lead to a statistically significant decrease in the proportion of the micron-sized fraction from 13.9±9.2 to 1.9±0 (Figure S1, SI). This fraction was further reduced to 0 % in samples with ultrasonication.

To assess their suitability for animal studies, the aggregation stability of NPs was investigated over a 5-minute period, mimicking the time from suspension to administration. This study revealed that after 5 minutes of storage, the hydrodynamic diameter of the initial (IN) and ground (GM) particles increased by approximately 200 nm and 400 nm, respectively. Conversely, for particles prepared by grinding and ultrasonication (GM+US), the hydrodynamic diameter decreased by about 200 nm, a change attributed to contribution of newly observed 204 nm fraction (5.5 %). Importantly, holding the ultrasonically dispersed particles for 5 minutes did not result in the appearance of a micron fraction. This observation suggest that these samples are sufficiently stable for use in *in vivo* applications.

Conclusions

This work investigated the effect of homogenization treatment on the crystal structure and oxidative performance of NPs. The results revealed that the NPs initially formed within MOF-cylinder as surface Fe_3O_4-spheric samples. However, after homogenization treatment involving mortar grinding and ultrasonication (3 min at 30 kHz and 37 °C), these particles transformed into compact, near-spherical structures. Crucially, the oxidative behavior of NPs was remarkably improved by both milling and ultrasonic homogenization. The enhanced oxidative performance of the homogenized samples is primarily attributed to the increased release of Fe^{2+}/Fe^{3+} ions. Furthermore, the ultrasonically-treated samples exhibited sufficiently low hydrodynamic diameters and higher stability compared to the initial samples. These findings underscore that the influence of routine sample preparation operations on the structure and functional properties of NPs cannot be underestimated.

Supporting Information

The Supporting Information is available free at https://ejc.buketov.edu.kz/ejc/article/view/606/355

Funding

The study was supported by a grant from the Russian Science Foundation (No. 22-73-10222-P, "Preparation, physicochemical characterization and pro-oxidant properties of new iron-containing mesoporous materials", https://rscf.ru/en/project/22-73-10222/).

*Author Information**

**The authors' names are presented in the following order: First Name, Middle Name and Last Name*

Lyubov Sergeevna Bondarenko — PhD (Chemistry), Associate Professor, Advanced Materials and Technologies for Aerospace Applications Department, Moscow Aviation Institute (National Research University), Volokolamskoe shosse, 4, 125080, Moscow, Russia; e-mail: l.s.bondarenko92@gmail.com; https://orcid.org/0000-0002-3107-0648

Artur Albertovich Dzeranov — Assistant Lecturer, Advanced Materials and Technologies for Aerospace Applications Department, Moscow Aviation Institute (National Research University), Volokolamskoe shosse, 4, 125080, Moscow, Russia; e-mail: arturdzeranov99@gmail.com; https://orcid.org/0000-0003-3240-9321

Natalya Sergeevna Tropskaya — PhD, DSc (Biology), Professor, Advanced Materials and Technologies for Aerospace Applications Department, Moscow Aviation Institute (National Research University), Volokolamskoe shosse, 4, 125080, Moscow, Russia; Head of Experimental Pathology Laboratory, Sklifosovsky Research Institute for Emergency Medicine, Bolshaya Sukharevskaya Square, 3/21, 107045, Moscow, Russia; e-mail: tropskayans@gmail.com; https://orcid.org/0000-0001-5870-9483

Kamila Asylbekovna Kydralieva (*corresponding author*) — PhD, DSc (Chemistry), Professor, Advanced Materials and Technologies for Aerospace Applications Department, Moscow Aviation Institute (National Research University), Volokolamskoe shosse, 4, 125080, Moscow, Russia; e-mail: kamila.kydralieva@gmail.com; https://orcid.org/0000-0002-4596-4140

Author Contributions

The manuscript was written through contributions of all authors. All authors have given approval to the final version of the manuscript. CRediT: **Lyubov Sergeevna Bondarenko** investigation, writing — original draft; **Artur Albertovich Dzeranov** investigation, formal analysis; **Natalya Sergeevna Tropskaya** resources; **Kamila Asylbekovna Kydralieva** writing — review & editing, supervision, conceptualization.

Acknowledgments

Special thanks to Professor Gulzhian Dzhardimalieva and Roza Baimuratova from the Federal Research Center for Problems of Chemical Physics and Medicinal Chemistry of the Russian Academy of Sciences for providing the samples.

Conflicts of Interest

The authors declare no conflict of interest.

References

1 Cherepanova, V.A., Gordeev, E.G., & Ananikov, V.P. (2025). Magnetic Stirring May Cause Irreproducible Results in Chemical Reactions. *JACS Au*, *5*(8), 3789–3798. https://doi.org/10.1021/jacsau.5c00412

2 Mirkin, C.A., Petrosko, S.H., Artzi, N., Aydin, K., Biaggne, A., Brinker, C.J., Bujold, K.E., Cao, Y.C., Chan, R.R., Chen, C., Chen, P.C., Chen, X., Chevalier, O.J.G.L., Choi, C.H.J., Crooks, R.M., Dravid, V.P., Du, J.S., Ebrahimi, S.B., Fan, H., Farha, O.K., Figg, C.A., Fink, T.D., Forsyth, C.M., Fuchs, H., Geiger, F.M., Gianneschi, N.C., Gibson, K.J., Ginger, D.S., Guo, S.S., Hanes, J.S., Hao, L., Huang, J., Hunter, B.M., Huo, F., Hwang, J., Jin, R., Kelley, S.O., Kempa, T.J., Kim, Y., Kudruk, S., Kumari, S., Landy, K.M., Lee, K.B., Leon, N.J., Li, J., Li, Y., Li, Z., Liu, B., Liu, G., Liu, X., Liz-Marzán, L.M., Lorch, J.H., Luo, T., Macfarlane, R.J., Millstone, J.E., Mrksich, M., Murphy, C.J., Naik, R.R., Nel, A.E., Oetheimer, C., Hedlund Orbeck, J.K., Park, S.J., Partridge, B.E., Peppas, N.A., Personick, M.L., Raj, A., Ramani, N., Ross, M.B., Ross, S.B., Sargent, E.H., Sengupta, T., Schatz, G.C., Seferos, D.S., Seideman, T., Seo, S.E., Shen, B., Shim, W., Shin, D., Simon, U., Sinegra, A.J., Smith, P.T., Spokoyny, A.M., Stang, P.J., Stegh, A.H., Stoddart, J.F., Swearer, D.F., Tan, W., Teplensky, M.H., Thaxton, C.S., Walt, D.R., Wang, M.X., Wang, Z., Wei, W.D., Weiss, P.S., Winegar, P.H., Xia, Y., Xie, Y., Xu, X., Yang, P., Yang, Y., Ye, Z., Yoon, K.R., Zhang, C., Zhang, H., Zhang, K., Zhang, L., Zhang, X., Zhang, Y., Zheng, Z., Zhou, W., Zhu, S. & Zhu, W. (2025). 33 Unresolved Questions in Nanoscience and Nanotechnology. *ACS Nano*, 19, 36, 31933–31968. https://doi.org/10.1021/acsnano.5c12854

3 Babayevska, N., Przysiecka, L., Iatsunskyi, I., Nowaczyk, G., Jarek, M., Janiszewska, E., & Jurga, S. (2023). Author Correction: ZnO size and shape effect on antibacterial activity and cytotoxicity profile. *Scientific reports*, *13*(1), 12465. https://doi.org/10.1038/s41598-023-39615-3

4 Zhang, B., Sai Lung, P., Zhao, S., Chu, Z., Chrzanowski, W., & Li, Q. (2017). Shape dependent cytotoxicity of PLGA-PEG nanoparticles on human cells. *Scientific reports*, *7*(1), 7315. https://doi.org/10.1038/s41598-017-07588-9

5 Subhan, M.A., Yalamarty, S.S.K., Filipczak, N., Parveen, F., & Torchilin, V.P. (2021). Recent Advances in Tumor Targeting via EPR Effect for Cancer Treatment. *Journal of personalized medicine*, *11*(6), 571. https://doi.org/10.3390/jpm11060571

6 Rizvi, S.A.A., & Saleh, A.M. (2018). Applications of nanoparticle systems in drug delivery technology. *Saudi pharmaceutical journal: SPJ: the official publication of the Saudi Pharmaceutical Society*, *26*(1), 64–70. https://doi.org/10.1016/j.jsps.2017.10.012

7 Öztürk, K., Kaplan, M., & Çalış, S. (2024). Effects of nanoparticle size, shape, and zeta potential on drug delivery. *International journal of pharmaceutics*, *666*, 124799. https://doi.org/10.1016/j.ijpharm.2024.124799

8 Bhatia, S. (2016). Natural Polymer Drug Delivery Systems. *Springer International Publishing*. https://doi.org/10.1007/978-3-319-41129-3

9 Bhardwaj, V., Kaushik, A., Khatib, Z.M., Nair, M., & McGoron, A.J. (2019). Recalcitrant Issues and New Frontiers in Nano-Pharmacology. *Frontiers in pharmacology*, *10*, 1369. https://doi.org/10.3389/fphar.2019.01369

10 Honary, S., & Zahir, F. (2013). Effect of Zeta Potential on the Properties of Nano-Drug Delivery Systems — A Review (Part 2). *Tropical Journal of Pharmaceutical Research*, *12*(2), 265–273. https://doi.org/10.4314/tjpr.v12i2.20

11 Ding, S., Khan, A. I., Cai, X., Song, Y., Lyu, Z., Du, D., Dutta, P., & Lin, Y. (2020). Overcoming blood-brain barrier transport: Advances in nanoparticle-based drug delivery strategies. *Materials today (Kidlington, England)*, *37*, 112–125. https://doi.org/10.1016/j.mattod.2020.02.001

12 Clogston, J.D., & Patri, A.K. (2011). Zeta potential measurement. *Methods in molecular biology (Clifton, N.J.)*, *697*, 63–70. https://doi.org/10.1007/978-1-60327-198-1_6

13 Mahbubul, I.M., Saidur, R., Amalina, M.A., Elcioglu, E.B., & Okutucu-Ozyurt, T. (2015). Effective ultrasonication process for better colloidal dispersion of nanofluid. *Ultrasonics sonochemistry*, *26*, 361–369. https://doi.org/10.1016/j.ultsonch.2015.01.005

14 Müller, R.H., Jacobs, C., & Kayser, O. (2001). Nanosuspensions as particulate drug formulations in therapy. Rationale for development and what we can expect for the future. *Advanced drug delivery reviews*, *47*(1), 3–19. https://doi.org/10.1016/s0169-409x(00)00118-6

15 Hwang, Y., Lee, J., Lee, J., Jeong, Y., Cheong, S., Ahn, Y.C., & Kim, S.H. (2008). Production and dispersion stability of nanoparticles in nanofluids. *Powder Technology*, *186*, 145–153. https://doi.org/10.1016/j.powtec.2007.11.020

16 Kamala Kumari, P.V. & Srinivasa Rao, Y. (2017). Nanosuspensions: A review. *International Journal of Pharmacy*, *7*(2), 77–89.

17 Taurozzi, J., Hackley, V. & Wiesner, M. (2012). Preparation of Nanoparticle Dispersions from Powdered Material Using Ultrasonic Disruption — Version 1.1. *National Institute of Standards and Technology*, *Gaithersburg*, MD. https://doi.org/10.6028/NIST.SP.1200-2

18 Sobenin, D.V., Solovov, R.D. & Ershov, B.G. (2026). Transformation of zerovalent iron nanoparticles in isopropanol into oxide particles: effect of water and air on mechanism and kinetics. *Journal of Molecular Liquids*, *447*, 129333. https://doi.org/10.1016/j.molliq.2026.129333

19 Taurozzi, J.S., Hackley, V.A., & Wiesner, M.R. (2011). Ultrasonic dispersion of nanoparticles for environmental, health and safety assessment—issues and recommendations. *Nanotoxicology*, *5*(4), 711–729. https://doi.org/10.3109/17435390.2010.528846

20 Mane, N.P., Rane, B.R. & Jain, A.S. (2024). Advances in Nanosuspension Technology: Current Trends and Future Horizons. *Nano Biomedicine and Engineering*, *16*(4), 574–587. https://doi.org/10.26599/NBE.2024.9290092

21 Jacob, S., Nair, A. B., & Shah, J. (2020). Emerging role of nanosuspensions in drug delivery systems. *Biomaterials research*, *24*, 3. https://doi.org/10.1186/s40824-020-0184-8

22 Li, H., Zhu, M., Pang, Y., Du, H. & Liu, T. (2016). Influences of ultrasonic irradiation on the morphology and structure of nanoporous Co nanoparticles during chemical dealloying. *Progress in Natural Science: Materials International*, *26*, 562–566. https://doi.org/10.1016/j.pnsc.2016.12.002

23 Zhang, X., Jiang, X., Qu, S., Zhang, H., Yang, W., Lu, W. (2022). Effects of ultrasonication on the microstructures and mechanical properties of carbon nanotube films and their based composites. *Composites Science and Technology*, *221*, 109136. https://doi.org/10.1016/j.compscitech.2021.109136

24 Li, Y. -H., Wang, C.-C., Yi, X.-H. & Chu, H.-Y. (2023). UiO-66(Zr)-based functional materials for water purification: An updated review. *Environmental Functional Materials*, *2*(2), 93–132. https://doi.org/10.1016/j.efmat.2024.02.001

25 Lin, Y., Min, K., Ma, W., Yang, X., Lu, D., Lin, Z., Liu Q. & Jiang, G. (2024). Probing the stability of metal–organic frameworks by structure-responsive mass spectrometry imaging. *Chemical Science*, *15*, 3698–3706. https://doi.org/10.1039/D4SC00021H

26 Bondarenko, L., Baimuratova, R., Dzeranov, A., Pankratov, D., Kicheeva, A., Sushko, E., Kudryasheva, N., Valeev, R., Tropskaya, N., Dzhardimalieva, G. & Kydralieva, K. (2024). Fenton reaction-driven pro-oxidant synergy of ascorbic acid and iron oxide nanoparticles in MIL-88B(Fe). *New Journal of Chemistry*, 48, 10142–10160. https://doi.org/10.1039/D4NJ00963K

27 Elmore, W.C. (1938). Ferromagnetic Colloid for Studying Magnetic Structures. *Physical Review*, *54*, 309–310. https://doi.org/10.1103/PhysRev.54.309

28 Xu, X., Ma, J., Wang, A. & Zheng, N. (2023). N-Sulfonyl amidine polypeptides: new polymeric biomaterials with conformation transition responsive to tumor acidity. *Chemical Science*, 15(5), 1769–1781. https://doi.org/10.1039/d3sc05504c

29 Sun, R., Wang, Y., Shi, W., Zhang, H., Liu, J. & He, W. (2024). Acidity-Triggered "Sticky Spotlight": CCK2R-targeted TME-sensitive NIR fluorescent probes for tumor imaging *in vivo*. *Bioconjugate Chemistry*, *35*(4), 528–539. https://doi.org/10.1021/acs.bioconjchem.4c00040

30 Liu, Y., Huang, S., Sun, H.J., Liu, Y., Liang, L., Nan, Q., Wang, T., Chen, Z., Tang, J., Hu, C. & Zhao, J.R. (2023). Amorphous Cu-Mn hopcalite as novel Fenton-like catalyst for H_2O_2-activated degradation of tetracycline at circumneutral pH. *Journal of Science: Advanced Materials and Devices*, *8*(3), 100603. https://doi.org/10.1016/j.jsamd.2023.100603

31 Maniakova, G. & Rizzo, L. (2023). Pharmaceuticals degradation and pathogens inactivation in municipal wastewater: A comparison among UVC photo-Fenton with chelating agents, UVC/H_2O_2 and ozonation. *Journal of Environmental Chemical Engineering*, *11*(6), 111356. https://doi.org/10.1016/j.jece.2023.111356

32 Schwaminger, S.P., Syhr, C., & Berensmeier, S. (2020). Controlled Synthesis of Magnetic Iron Oxide Nanoparticles: Magnetite or Maghemite? *Crystals*, *10*, 214. https://doi.org/10.3390/cryst10030214

33 Gorski, C.A., & Scherer, M.M. (2010). Determination of nanoparticulate magnetite stoichiometry by Mössbauer spectroscopy, acidic dissolution, and powder X-ray diffraction: A critical review. *American Mineralogist*, *95*(7), 1017–1026. https://doi.org/10.2138/am.2010.3435

34 Bogart, L.K., Blanco-Andujar, C. & Pankhurst, Q.A. (2018). Environmental oxidative aging of iron oxide nanoparticles. *Applied Physics Letters*, *113*, 133701. https://doi.org/10.1063/1.5050217

35 Saber Braim, F., Noor Ashikin Nik Ab Razak, N., Abdul Aziz, A., Qasim Ismael, L., & Kayode Sodipo, B. (2022). Ultrasound assisted chitosan coated iron oxide nanoparticles: Influence of ultrasonic irradiation on the crystallinity, stability, toxicity and magnetization of the functionalized nanoparticles. *Ultrasonics sonochemistry*, *88*, 106072. https://doi.org/10.1016/j.ultsonch.2022.106072

36 Stolyar, S.V., Bayukov, O.A., Yaroslavtsev, R.N., Knyazev, Yu.V., Ladygina, V.P., Gerasimova, Yu.V. & Iskhakov, R.S. (2019). Ion Reduction in Iron Oxide and Oxihydroxide Nanoparticles During Ultrasonic Treatment. *Advanced Powder Technology*, *30*, 2620–2625. https://doi.org/10.1016/j.apt.2019.08.009

37 Kim, D., Lee, G., Oh, S. & Oh, M. (2019). Unbalanced MOF-on-MOF growth for the production of a lopsided core–shell of MIL-88B@MIL-88A with mismatched cell parameters. *Chemical Communications*. *55*, 43–46. https://doi.org/10.1039/C8CC08456D

38 Bondarenko, L., Baimuratova, R., Reindl, M., Zach, V., Dzeranov, A., Pankratov, D., Kydralieva, K., Dzhardimalieva, G., Kolb, D., Wagner, F.E., Schwaminger, S.P. (2024). Dramatic change in the properties of magnetite-modified MOF particles depending on the synthesis approach. *Heliyon*, *10*, 6, e27640. https://doi.org/10.1016/j.heliyon.2024.e27640

39 Pukazhselvan, D., Granadeiro, C.M., Loureiro, F.J., Shaula, A.L., Mikhalev, S.M., Goncalves, G., & Fagg, D.P. (2023). Comparative analyses of MIL-88B (Fe) and MIL-100 (Fe) metal organic frameworks as active anode materials for Li ion batteries. *Electrochimica Acta*, *465*, 142989. https://doi.org/10.1016/j.electacta.2023.142989

40 Ramos, M.D.N., Silva, G.L.S., Lessa, T.L. & Aguiar, A. (2022). Study of kinetic parameters related to dyes oxidation in ascorbic acid-mediated Fenton processes. *Process Safety and Environmental Protection*, *168*, 1131–1141. https://doi.org/10.1016/j.psep.2022.10.083

41 Gogate, P. R., & Patil, P. N. (2015). Combined treatment technology based on synergism between hydrodynamic cavitation and advanced oxidation processes. *Ultrasonics sonochemistry*, *25*, 60–69. https://doi.org/10.1016/j.ultsonch.2014.08.016

42 Pouran, S.R., Aziz, A.R., & Daud, W.M. (2015). Review on the main advances in photo-Fenton oxidation system for recalcitrant wastewaters. *Journal of Industrial and Engineering Chemistry*, *21*, 53–69. https://doi.org/10.1016/j.jiec.2014.05.005

43 Li, J., Zhao, L., Qin, L., Tian, X., Wang, A., Zhou, Y. & Chen, Y. (2016). Removal of refractory organics in nanofiltration concentrates of municipal solid waste leachate treatment plants by combined Fenton oxidative-coagulation with photo–Fenton processes. *Chemosphere*, *146*, 442–449. https://doi.org/10.1016/j.chemosphere.2015.12.069

44 Pouran, S.R., Raman, A.A., & Daud, W.M. (2014). Review on the application of modified iron oxides as heterogeneous catalysts in Fenton reactions. *Journal of Cleaner Production*, *64*, 24–35. https://doi.org/10.1016/j.jclepro.2013.09.013

45 Pouran, S.R., Aziz, A.A., Daud, W.M.A.W., & Embong, Z. (2015). Niobium substituted magnetite as a strong heterogeneous Fenton catalyst for wastewater treatment. *Applied Surface Science*, *351*, 175–187. https://doi.org/10.1016/j.apsusc.2015.05.131

46 Costa, R.C., Lelis, M.F.F., Oliveira, L.C.A., Fabris, J.D., Ardisson, J.D., Rios, R.R.V.A., Silva, C.N. & Lago, R. M. (2006). Novel active heterogeneous Fenton system based on Fe3− xMxO4 (Fe, Co, Mn, Ni): The role of M^{2+} species on the reactivity towards H_2O_2 reactions. *Journal of hazardous materials*, *129*(1–3), 171–178. https://doi.org/10.1016/j.jhazmat.2005.08.028

47 Magalhães, F., Pereira, M.C., Botrel, S.E.C., Fabris, J.D., Macedo, W.A., Mendonça, R., Lago, R.M. & Oliveira, L.C.A. (2007). Cr-containing magnetites $Fe_{3-x}Cr_xO_4$: The role of Cr^{3+} and Fe^{2+} on the stability and reactivity towards H_2O_2 reactions. *Applied Catalysis A: General*, *332*, 115–123. https://doi.org/10.1016/j.apcata.2007.08.002

48 Liang, X., Zhong, Y., He, H., Yuan, P., Zhu, J., Zhu, S., & Jiang, Z. (2012). The application of chromium substituted magnetite as heterogeneous Fenton catalyst for the degradation of aqueous cationic and anionic dyes. *Chemical Engineering Journal*, *191*, 177–184. https://doi.org/10.1016/j.cej.2012.03.001

49 Pouran, S.R., Bayrami, A., Aziz, A.A., Daud, W.M.A.W., & Shafeeyan, M.S. (2016). Ultrasound and UV assisted Fenton treatment of recalcitrant wastewaters using transition metal-substituted-magnetite nanoparticles. *Journal of Molecular Liquids*, *222*, 1076–1084. https://doi.org/10.1016/j.molliq.2016.07.120